Persistent clock of turbulent thermal convection

Lázaro Martínez-Ortíz, Youri H. Lemm, Herman J. H. Clercx, and Rudie P. J. Kunnen*
Fluids and Flows Group, Department of Applied Physics and Science Education and J. M. Burgers Center for Fluid Dynamics, Eindhoven University of Technology, P.O. Box 513, 5600 MB Eindhoven, The Netherlands

(Received 12 December 2025; accepted 17 February 2026; published 19 March 2026)

The large-scale circulation (LSC) of turbulent convection is a prominent feature of its dynamics and forms the basis for descriptive theories. We show, using experimental and numerical results from thermal convection in a cylindrical cell, that the LSC possesses a persistent internal "clock": its pulsating velocity as a function of time is described by a constant value of the parameter $U/(lf)$, where U is the mean velocity, f is the pulsation frequency, and l is the characteristic length scale. By introducing a narrow sidewall barrier, we can trip the LSC, forming a pair of interconnected rolls stacked above and below the barrier. They independently exhibit the same value for the ratio $U/(lf)$, even for vertically asymmetric pairs, indicating signs of synchrony. Thus, this parameter establishes a direct connection between plume-shedding dynamics and the flow topology.

DOI: 10.1103/tvt2-5523

I. INTRODUCTION

For over a century, a fluid layer heated from below and cooled from above has served as the established model of buoyancy-driven convection, commonly known as Rayleigh-Bénard convection (RBC) [1,2]. A hallmark of turbulent RBC in confined geometries is the emergence of a large-scale circulation (LSC) [3], with hot fluid rising on one wall and cold fluid sinking on the opposite, organizing into a single cell-spanning roll. The LSC shows a remarkable rich dynamical variability [4–7], while its large-scale structure persists [8–11]. This resilience provides the foundation for phenomenological models [3,12,13], which explicitly rely on the presence and structure of the LSC to make their predictions [3,4,14–17]. However, early studies employing strong obstructions to disrupt the LSC [18–20] challenged these theoretical expectations, showing that heat transport was largely insensitive to flow structure.

The LSC arises from the collective organization of hot and cold thermal plumes, which tend to cluster and move synchronously, producing periodic near-wall temperature and velocity signals [4,21]. Plume circulation and mean wind have been proposed to be mutually slaved [22,23], but the precise nature of this coupling remains unclear; whether the LSC drives the motion of the plumes or is itself sustained by their buoyant driving remains an open question.

In this work, we address the problem by directly controlling the flow topology. We show that a small perturbation (a narrow ring-shaped sidewall barrier at midheight) suffices to reorganize the LSC. At low forcing, it remains stable, but at higher driving it splits into a pair of interconnected counter-rotating circulations with stepwise boundary-layer thinning. In this distinct topology, the characteristic velocity retains its original scaling, while the pulsation frequency of the flow doubles. A universal relation emerges, linking the circulation timescale to the plume-shedding frequency. The pair of rolls are dynamically linked, with frequencies connected through the same relation that persists even when they are asymmetric. These results expose a direct quantitative connection between plume dynamics and mean flow, opening avenues for using RBC to probe the interplay between circulation structure, synchrony, and turbulence.

II. EXPERIMENTAL AND NUMERICAL SETUP

Experiments are carried out on a cylindrical sample filled with water at a mean temperature $\overline{T} \approx 30\ ^\circ$C. The cell has diameter and height $D = L = 0.2$ m (aspect ratio $\Gamma = 1$), with copper top and bottom plates and a Plexiglas sidewall. A ring-shaped Plexiglas barrier with width $d = 10$ mm and height $h = 8$ mm is mounted around the sidewall [see Fig. 1(a)], positioned at heights $L/2$, $L/3$, or $L/4$. The convective flow is described by the Rayleigh number $\mathrm{Ra} = \alpha g \Delta L^3/(\nu\kappa)$, which quantifies the balance between buoyancy and dissipative effects, and the Prandtl number $\mathrm{Pr} = \nu/\kappa$, the ratio of momentum to thermal diffusivity. Here, α is the thermal expansion coefficient, g is gravity, Δ is the imposed temperature difference, ν is the kinematic viscosity, and $\kappa$is the thermal diffusivity. The experiments cover the range $3.8 \times 10^8 \leqslant \mathrm{Ra} \leqslant 4.7 \times 10^9$, with an average Prandtl number of $\mathrm{Pr} \approx 5.8$.

The flow field is measured using Particle Image Velocimetry (PIV) [24]. To reduce optical distortions caused by the cylindrical sidewall, a square Plexiglas jacket filled with water is placed around the cell. The PIV system employs a vertically aligned laser sheet of 2 mm thickness, positioned at the midplane of the cell, $y = L/2$, and a high-resolution camera (2560×2048 pixels) that captures the motion of 20-μm-diameter polyamide tracer particles at 15 frames per second.

*Contact author: r.p.j.kunnen@tue.nl

Published by the American Physical Society under the terms of the Creative Commons Attribution 4.0 International license. Further distribution of this work must maintain attribution to the author(s) and the published article's title, journal citation, and DOI.

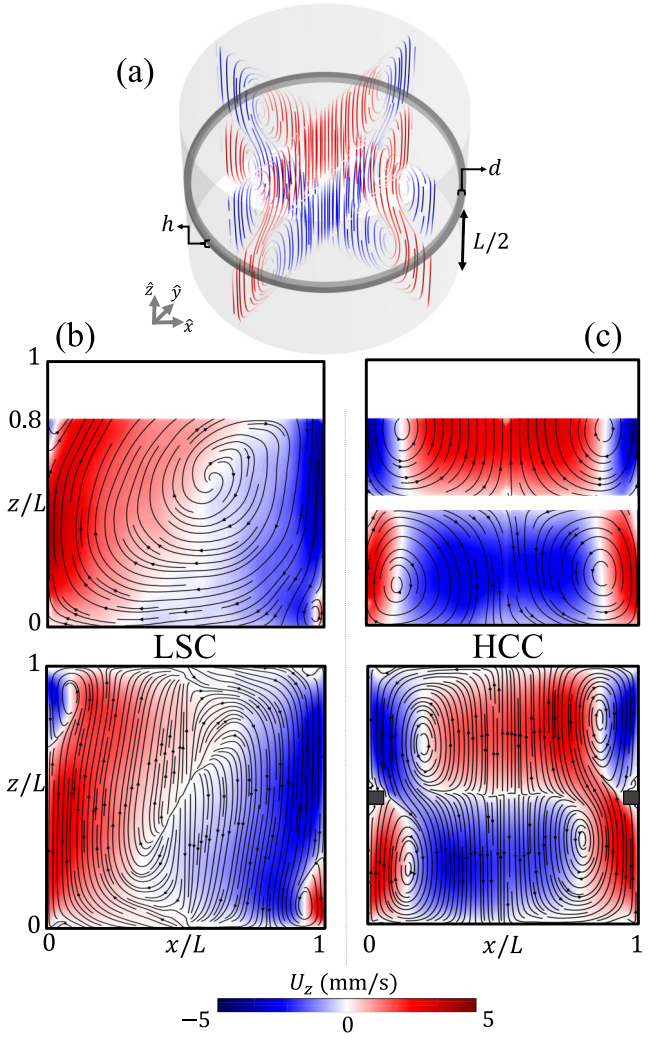


FIG. 1. (a) Sketch of the $\Gamma = 1$ cylindrical cell, where a narrow ring-shaped barrier is mounted at midheight along the sidewall; it can be removed or repositioned. Oblique views of streamlines from two perpendicular cross sections reveal the "nearly" axisymmetric flow structures inside. (b), (c) Measurements of the mean vertical velocity U_z overlaid with two-dimensional (2D) streamlines. The field of view covers about 80% of the full height L. (b) Shown from experimental data (top) and numerical simulation (bottom), for a smooth sidewall, the LSC dominates. (c) With the barrier, the LSC is replaced by a four-roll structure within the measurement field, the Half-Cell Circulation (HCC). In the experiments, the barrier appears as a white band where it obstructs a small portion of the field. All data are at $\mathrm{Ra} = 1.03 \times 10^9$.

We perform two sets of experiments. The first set aims to cover as much of the velocity field as possible to draw conclusions about the overall flow topology. Due to experimental constraints, these measurements do not cover the full vertical extent of the cell; approximately 20% of the cross-sectional area near the top plate remains inaccessible. However, the symmetries of the system allow us to draw robust conclusions from the accessible portion. The second set focuses on measuring the flow very close to the container sidewall to resolve the viscous boundary layer. For this purpose, we position the camera closer to the wall to achieve better spatial resolution. Each velocity field is reconstructed on a 79×63 vector grid, yielding a spatial resolution of 2.4 mm for the first set and 1.5 mm for the second. No specific control is applied to the azimuthal orientation of the LSC with respect to the PIV plane. The LSC is allowed to freely orient, and measurements are taken while ensuring it is prominently captured. Experiments last at most 10 min, during which rare reorientations, cessations, and rotations of the LSC [5,7] are not observed and do not affect the results.

To complement the experiments and gain access to the full three-dimensional velocity and temperature fields, we conduct direct numerical simulation (DNS) of the incompressible Navier-Stokes and heat equations for a Boussinesq fluid. These simulations also allow us to directly quantify the convective heat transfer through the Nusselt number, $\mathrm{Nu} = JL/(\kappa\Delta)$, where J is the heat flux, expressing the efficiency of convective heat transfer. The formulation is nondimensionalized using the temperature difference Δ, height L, and the free-fall velocity $U_{\mathrm{ff}} = \sqrt{\alpha g \Delta L}$. No-slip velocity conditions are applied on all boundaries, the sidewalls are thermally insulating, while the top and bottom plates are held at fixed temperatures. The equations are discretized on a cylindrical grid using a second-order finite-difference scheme with third-order Runge-Kutta time stepping. Further details on the numerical scheme can be found in Refs. [25,26]. The simulations are performed with parameters that match those of the experiments for three Ra values: 3.8×10^8, 1.03×10^9, and 5.0×10^9. To implement the ring-shaped barrier numerically, we employ the so-called volume penalization method [27], which introduces an additional term in the Navier-Stokes equations that is active only within the barrier region and forces the velocity toward zero there, thus mimicking an impermeable boundary. The flow is governed by the Navier-Stokes equation [Eq. (1)], incompressibility [Eq. (2)], and the heat equation [Eq. (3)], written as follows:

$$\frac{\partial \mathbf{u}}{\partial t} + (\mathbf{u}\cdot\boldsymbol{\nabla})\mathbf{u} = -\boldsymbol{\nabla} p + \sqrt{\frac{\mathrm{Pr}}{\mathrm{Ra}}}\nabla^2\mathbf{u} + \theta\hat{z} - \chi\,\zeta\,\mathbf{u}, \tag{1}$$

$$\boldsymbol{\nabla}\cdot\mathbf{u} = 0, \tag{2}$$

$$\frac{\partial \theta}{\partial t} + (\mathbf{u}\cdot\boldsymbol{\nabla})\theta = \frac{1}{\sqrt{\mathrm{PrRa}}}\nabla^2\theta. \tag{3}$$

Here, $\mathbf{u}$ denotes the velocity field, θ is the temperature, p is the pressure, t is the time, and $\hat{z}$ is the vertical unit vector. The additional term $(-\chi\,\zeta\,\mathbf{u})$ accounts only for the barrier, where the mask function $\chi = 1$ inside the barrier and $\chi = 0$ outside the barrier. The parameter ζ controls the strength of the penalization (we set $\zeta = 100$ for all simulation runs). Heat diffusion in the barrier is solved in the same manner as in the fluid, using the same thermal diffusion coefficient.

III. RESULTS AND DISCUSSION

Figures 1(b) and 1(c) shows the mean vertical velocity field from experimental measurements (top) and from DNS (bottom) under identical conditions ($\mathrm{Ra} = 1.03 \times 10^9$); the only difference is the presence or absence of the barrier. The vertical velocity field is overlaid with streamlines. Generally good agreement is observed between experiment and simulation. In the smooth-wall configuration [Fig. 1(b)], the flow

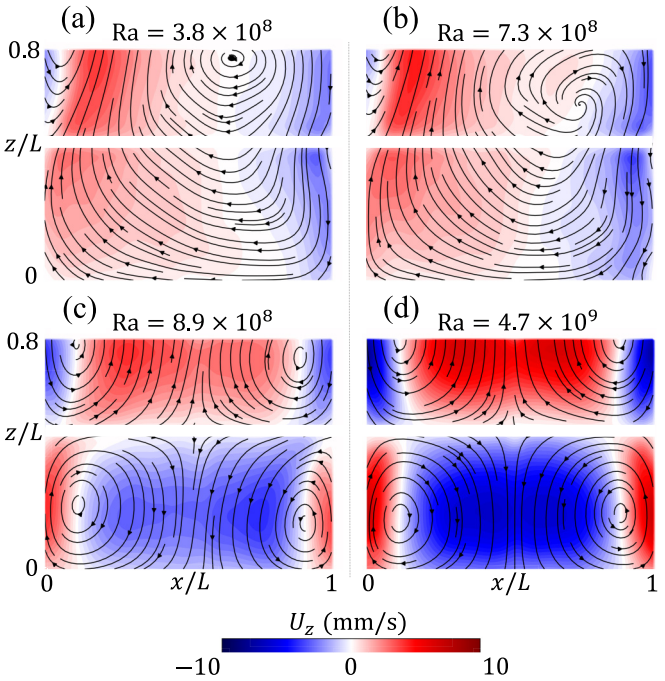


FIG. 2. Flow topology at different driving strengths (Ra), shown through mean vertical velocity (U_z) fields overlaid with 2D streamlines for the barrier case. (a), (b) At lower thermal driving, the LSC persists as the dominant flow component. (c) As driving increases the flow breaks into four rolls in the vertical plane. (d) The HCC remains robust even at higher levels of turbulence.

is dominated by a single large-scale convective roll, with upwelling and downwelling on opposing sides of the cell (the LSC), two smaller counterrotating secondary rolls appear near diagonally opposite corners, consistent with the expected structure in this regime. The LSC spans the entire length of the container, with a characteristic scale comparable to the size of the system L. Alternatively, when a barrier is introduced at midheight ($L/2$), the flow reorganizes dramatically [Fig. 1(c)]. The classical single-roll LSC structure is disrupted, and the velocity field exhibits a four-roll structure in the vertical midplane. The location of the barrier sets the scale of the emerging flow structures by splitting the domain. Rather than a single full-length circulation, two half-sized pairs of counterrotating vortices form above and below the barrier, extending from the horizontal top and bottom plates to the sidewall obstruction at $L/2$. Figure 1(a) shows that the modified flow is nearly axisymmetric, forming an interconnected pair of donutlike, counterrotating vortices above and below the barrier. These pairs interconnect to produce figure-eight-shaped structures in every vertical plane, linked in a complex three-dimensional pattern. We refer to the top (bottom) vortex pair as an HCC.

As a step in further exploring the underlying causes of the observed changes in flow structure, we measured velocity fields at various intensities of thermal forcing. Figure 2 highlights the flow topology for different Ra through 2D streamlines. Notably, the LSC remains the dominant flow feature at low thermal driving, Ra $= 3.8 \times 10^8$ and 7.3×10^8 [Figs. 2(a) and 2(b)], circulating over the barrier as if it were unobtrusive. As Ra increases, a transition to the HCC

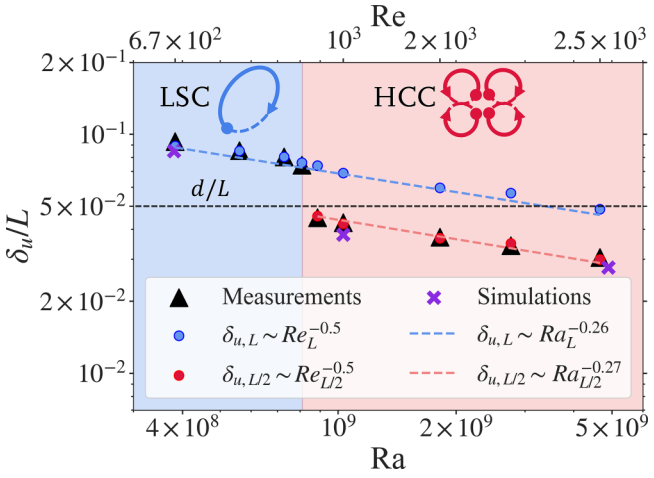


FIG. 3. Normalized BL thickness as a function of Ra and Re. In the blue-shaded region we observe a single LSC; in the pink-shaded region, we find two stacked HCCs. Black triangles mark direct measurements from the velocity profiles, using the maximum-velocity position relative to the wall. Circular markers indicate the Reynolds-number scaling laws using the measured $U_{\max}$; blue points use the classical definition Re_L and red circles use the rescaled $\mathrm{Re}_{L/2}$. Blue and red dashed lines represent the scaling laws based on Ra_L and $\mathrm{Ra}_{L/2}$, respectively. The black dashed line marks the position of the normalized barrier width, $d/L = 0.05$.

is observed after Ra $\approx 8 \times 10^8$ [Fig. 2(c)]. This distinct flow topology persists as the turbulence intensifies, observed up to Ra $= 4.7 \times 10^9$ [Fig. 2(d)]. This shows that the LSC can be disrupted, but only when the barrier length becomes a noticeable perturbation to the system; below this threshold, the LSC structure persists despite the obstacle.

The origin of this transition is examined by focusing on the viscous boundary layers (BLs), which are central to momentum and heat transport [3,12]. Near the boundaries, the time-averaged wall-parallel velocity component $U_\parallel = \langle u_\parallel(t) \rangle$ shows the classical Prandtl-Blasius (PB) structure: linear growth from the wall, a peak $U_{\max}$ at distance δ_u, and a gradual decay toward bulk values [3,28–31]. Here, we adopt this measure for the viscous boundary-layer thickness; i.e., δ_u is the distance from the wall to the peak vertical velocity $U_{\max}$ (see Fig. 7 in the Appendix).

Building on this foundation, Grossmann-Lohse (GL) theory [3,12] offers a unified description of turbulent thermal convection by treating the bulk and boundary layers (BLs) separately. A key assumption is that the kinetic BL obeys Blasius-type scaling, with $\delta_u/L \propto \mathrm{Re}^{-1/2}$, where $\mathrm{Re} = U_{\max} L/\nu$ is the Reynolds number. Consistent with this, experiments support a power-law dependence of δ_u on thermal forcing, with $\delta_u/L \propto \mathrm{Ra}^{-0.27\pm0.01}$ [3,32]. This scaling implies a progressive thinning of the BL with increasing thermal forcing and has been validated over a wide range of parameters [32,33].

Figure 3 shows the measured viscous boundary-layer thickness, δ_u, as a function of Ra and Re. At low forcing (Ra $\lesssim 8 \times 10^8$), both experiments and simulations follow the classical scaling predictions; we refer to this BL thickness as $\delta_{u,L}$. For Ra $\gtrsim 8 \times 10^8$, where the flow-structure transition occurs, δ_u exhibits a clear steplike deviation from

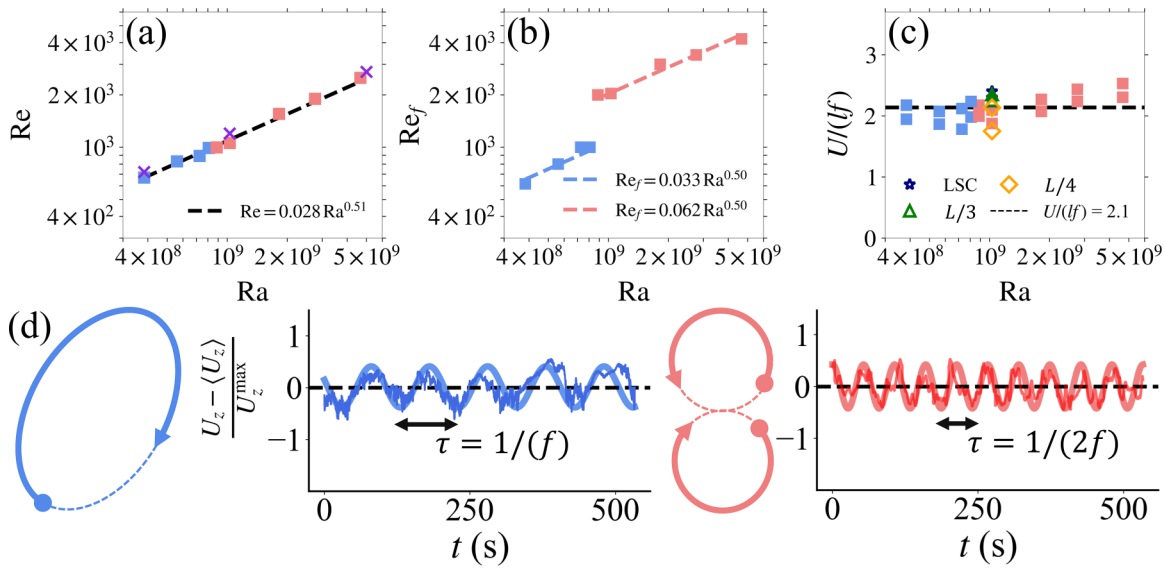


FIG. 4. (a) Re as a function of Ra for the barrier case. Squares denote experimental measurements (blue for LSC, pink for HCC), purple crosses indicate DNS results, and the dashed line is a fit. (b) Re_f as a function of Ra for the barrier case (dashed blue and pink lines represent the fits corresponding to the LSC and HCC states). (c) Dependence of U/lf on Ra. The two points per Ra correspond to measurements taken at the left/right sides when the LSC is dominant and at the top/bottom rolls after the transition (see Fig. 8 in the Appendix). The horizontal discontinuous line represents the fitted value $c = 2.1$. Open symbols for $\mathrm{Ra} = 1.03 \times 10^9$ correspond to cases where the barrier is not at $L/2$: LSC (without the barrier), $L/3$, and $L/4$. (d) Time series of near-wall velocity at $\mathrm{Ra} = 1.03 \times 10^9$ in nonbarrier and barrier cases (dark-shaded curves). After the transition, the flow pulsates at a higher frequency. The light-shaded lines correspond to the dominant frequency component of the signal's Fourier decomposition.

the classical behavior: the boundary layer becomes significantly thinner than predicted by the PB and GL theories and remains consistently below the barrier width; we refer to this BL thickness after the transitions as $\delta_{u,L/2}$. This observation indicates that the transition is triggered when the thickness of the viscous boundary layers, $\delta_{u,L}$, shrinks to the point of becoming comparable to the barrier width, $d/L = 0.05$. After the transition, the barrier dictates the boundary-layer thickness, which remains below d/L. Equivalently, the transition can be viewed as occurring when $\delta_{u,L/2} \lesssim d/L$, i.e., when the thinner boundary layer fits within the barrier width; once $\delta_{u,L/2}$ grows beyond the barrier width, the LSC is restored. We attribute this deviation to the observed change in the flow structure, from a single large-scale roll to two half-length structures, effectively reducing the characteristic length scale from L (blue-shaded region on the left of Fig. 3) to $L/2$ (pink-shaded region on the right of Fig. 3). To account for this change, the dimensionless numbers are rescaled using the reduced effective length, such that $\mathrm{Re}_{L/2} = U_{\max}(L/2)/\nu$ and $\mathrm{Ra}_{L/2} = \alpha g \Delta (L/2)^3/(\nu\kappa)$, while Re_L and Ra_L retain their standard definitions. With these modifications, the measurements realign with the classical scaling laws and recover comparable prefactors. Specifically, when the LSC remains the dominant flow component, we find $\delta_{u,L} = (15.0 \pm 1.0)\,\mathrm{Ra}_L^{-0.26\pm0.01} L$ and $\delta_{u,L} = (2.3 \pm 0.1)\,\mathrm{Re}_L^{-0.50\pm0.01} L$, as indicated by the blue dashed line and circles in Fig. 3. After the transition, a slightly steeper scaling is recovered for Ra, $\delta_{u,L/2} = (13.5 \pm 1.0)\,\mathrm{Ra}_{L/2}^{-0.27\pm0.01} L/2$, which remains consistent within the statistical error, and for Re, $\delta_{u,L/2} = (2.1 \pm 0.1)\,\mathrm{Re}_{L/2}^{-0.50\pm0.01} L/2$, as shown by the red dashed lines and circles in Fig. 3.

So far, our arguments have relied solely on the shift in the characteristic system scale. Examining the Re–Ra dependence (without applying any additional rescaling) provides further support for recovering the scaling laws using the reduced scale $(L/2)$. Figure 4(a) shows this relationship, where blue squares represent the flow before the transition and pink squares correspond to the flow after the transition. A power law, $\mathrm{Re}_L = (0.028 \pm 0.003)\,\mathrm{Ra}_L^{0.51\pm0.02}$, fits the data, in agreement with classical scalings [3,32]. This indicates that the characteristic velocity in the flow remains $U_{\max}$, as in the case without barriers, so the only significant change in the system is in the length scale.

The Reynolds number can also be characterized using the pulsation frequency f. This frequency can be extracted from near-wall temperature or velocity time series, where a periodic signal arises due to the coupling between boundary-layer instabilities (leading to the release of thermal plumes) and the slow convective motion of the LSC. In this scenario, the plumes and the LSC are mutually slaved [4,22,23,34]. Using this connection, one can define a frequency-based Reynolds number, $\mathrm{Re}_f = cfL^2/\nu$, which has been reported to exhibit values and scaling similar to the velocity-based Reynolds number with scaling constant $c = 2$, though $c(\mathrm{Ra})$ may rise beyond 2 for larger Ra [3,34,35].

In our case, near-wall velocity time series are extracted from the PIV measurements using small regions of interest placed close to the sidewalls. These regions serve as "virtual probes" from which the velocity signals are obtained (see Fig. 8 in the Appendix). Fourier analysis of these signals is then performed to determine their characteristic frequencies (see Figs. 4(d) and 8). After the flow-structure transition, we observe a surprising effect: the frequency doubles compared

to the expected value, resulting in a step increase in Re_f [Figs. 4(b) and 4(d)]. This behavior can also be understood from the reduction of the effective length scale in the system. Since the characteristic velocity can be expressed as $U_{\max} = c(\mathrm{Ra})Lf \approx 2Lf$, halving the length of the circulation path to $L/2$ requires doubling f to maintain the same velocity. This suggests that the flow adapts, pulsating at a higher frequency after its scale is reduced. Based on this observation and considering that previous studies have shown that the two definitions of the Reynolds number closely coincide over a wide range of parameters ($\mathrm{Re}_L = \mathrm{Re}_f$) [3,34–36], a conserved quantity can be identified, $U_i/(l_i f_i) = \text{const}$, where i denotes a flow structure of characteristic size l_i and velocity U_i. In Fig. 4(c), we show the Ra dependence of this ratio, which remains nearly constant at $c = 2.1$, displaying only a weak growth at higher turbulence levels. Physically, we argue that the plume-shedding frequency has a characteristic relationship with the LSC timescale $\tau = 1/f$, or equivalently to the shear rate $\dot{\gamma} = U_i/l_i$, so $\tau_i\dot{\gamma}_i = U_i/(l_i f_i) = \text{const}$. In other words, the "clock of circulation" persists according to the conserved dimensionless parameter $U_i/(l_i f_i)$ even when the flow topology undergoes significant changes. The weak upward trend in Fig. 4(c) is attributed to the reported increase in the effective circulation path with Ra [i.e., $c(\mathrm{Ra})$ growing beyond 2] [35]. Interestingly, this parameter is similar to the Strouhal number ($\mathrm{St}^{-1} = U/Lf$), which, in other contexts of oscillating flows, has also been observed to remain approximately constant over a wide range of Reynolds numbers [37].

To test the robustness of this relation, we create asymmetric top and bottom pairs by positioning the barrier at $z = L/3$ and $L/4$ (measured velocity fields with streamlines are shown in Fig. 8 in the Appendix), yielding structures with unequal characteristic lengths. Remarkably, the system exhibits signatures of generalized synchronization, where the state of one subsystem can be expressed as a function of the other, even if the two are not identical and have differing frequencies or phases [38]. In this case, the relation $U_t/(l_t f_t) = U_b/(l_b f_b)$ connects the top (t) and bottom (b) rolls. In the symmetric case, the velocities and length scales associated with t and b are equal, constraining the system to a state where both vortices circulate at similar frequencies, approximately twice that of the original no-barrier LSC, with their phases evolving in tandem [Figs. 4(d), 5(a), and 5(b)]. When $l_t > l_b$, asymmetries in velocity and length scales produce frequency differences, giving rise to major and minor rolls with mismatched frequencies ($f_t < f_b$) and phase evolutions [Fig. 5(c)]. The frequency mismatch and phase separation grow with the disparity between the rolls [Fig. 5(d)]. Strikingly, despite the asymmetry, the structures remain dynamically coupled [see Fig. 4(c) and Table I in the Appendix]. The observed coupling likely arises because the top-bottom and left-right rolls can be viewed as branches of a single distorted, figure-eight-axisymmetric circulation, continuously exchanging information rather than forming fully separated structures [19].

These observations are consistent with, and can be physically interpreted through, the role of thermal plumes, an idea introduced by Grossmann and Lohse to extend the GL theory [39]. They extended the theory by considering contributions of the thermal plumes and the turbulent background as an alternative equivalent decomposition to their original bulk/boundary-layer picture. Our results provide direct evidence for this picture and extend the theory. In their framework, plumes are detached fragments of the thermal boundary layer, and the plume-shedding frequency is set by the reheating of the boundary layer after such a detachment. Focusing on their analysis of the plume-shedding frequency [Eq. (37) of Ref. [39]], we apply the same arguments to our system. For the bottom flow structure (taken here as a representative example; the same reasoning applies to the top), once the

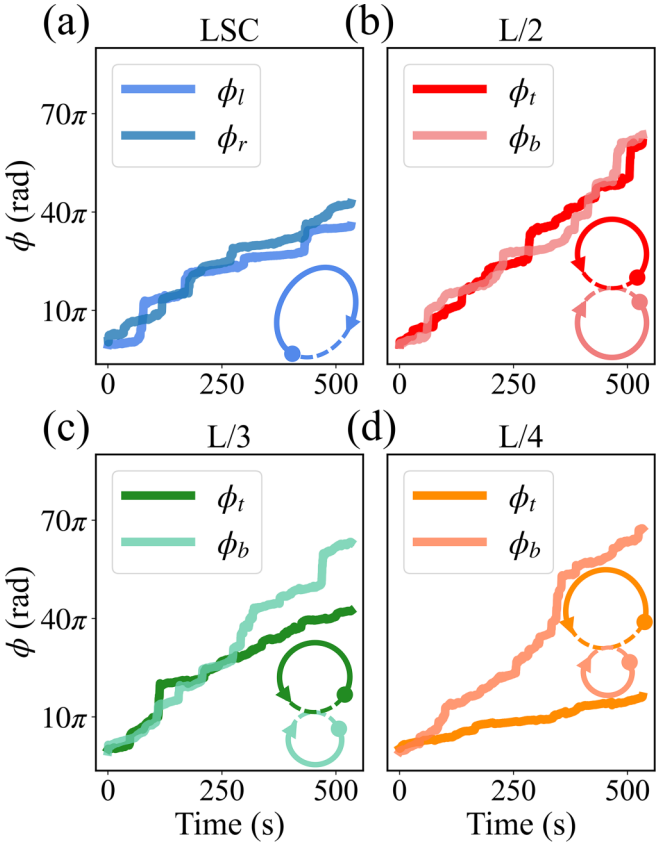


FIG. 5. Temporal evolution of the near-wall vertical velocity signal phase $\phi(t)$ for different barrier positions at $\mathrm{Ra} = 1.03 \times 10^9$. (a) Using the LSC as a reference, the signal phases on opposite walls evolve synchronously at the same frequency $2\pi f = \partial\phi/\partial t$, with $f_l \approx f_r = 10$ mHz (evaluated at left l and right r sides). (b) When the barrier is placed at $z = L/2$, the frequency doubles ($f_t \approx f_b = 20$ mHz), while the phases remain locked. (c) With barrier at $z = L/3$, the top and bottom rolls become asymmetric ($f_t = 10$ mHz, $f_b = 26$ mHz) and the phases no longer evolve together. (d) With barrier at $z = L/4$, the disparity increases ($f_t = 4$ mHz, $f_b = 28$ mHz).

TABLE I. Generalized synchronization relations.

Case	$\frac{U_t}{l_t f_t}\left(\frac{U_b}{l_b f_b}\right)^{-1}$	$\frac{U_t}{l_t f_{\mathrm{inst},t}}\left(\frac{U_b}{l_b f_{\mathrm{inst},b}}\right)^{-1}$
LSC	≈1.00	≈1.15
$L/2$	≈1.16	≈0.99
$L/3$	≈1.06	≈1.11
$L/4$	≈1.19	≈0.90

thermal boundary layer of thickness $\delta_{\theta,b}$ becomes unstable, a detached fragment is advected into the bulk by the mean flow, locally cooling the boundary layer, which must then reheat via the heat flux $J_b = \mathrm{Nu}_b \kappa \Delta / l_b$ (proportional to the heat transfer quantified by the local Nusselt number $\mathrm{Nu}_b \sim l_b/\delta_{\theta,b}$). The plume-shedding frequency is therefore set by the heat flux, $f_b \sim J_b/(\Delta\delta_{\theta,b}) = \kappa \mathrm{Nu}_b^2/l_b^2$. As $\mathrm{Nu}_b \sim \sqrt{C(\mathrm{Pr})\mathrm{Re}_b\mathrm{Pr}}$, where $C(\mathrm{Pr})$ is a constant that depends on the ratio of the thermal and viscous boundary-layer thicknesses, with different behavior in the low- and high-Prandtl-number regimes [39], one obtains $U_b/(l_b f_b) \sim C(\mathrm{Pr})$. The same analysis can be carried out for the top flow structure. This is precisely the relation observed in our results [Fig. 4(c)]. The underlying physical picture, in agreement with Villermaux's early work [4], is that detached thermal instabilities are advected by the LSC and, upon impinging on the upper thermal boundary layer, induce a rapid distortion that triggers the formation of a cold plume. The plume is then slowly advected downward, where the same mechanism is repeated. In our system, this picture remains valid after the scale shrinks: the same arguments can be applied independently to the top and bottom half-sized rolls, leading to the same physical interpretation.

These results are consistent with the alternative picture based on the length of the trajectory of a traveling plume [35], which also sheds light on the observed coupling mechanism. When a plume-shedding (detachment) event occurs, it generates a pulse that propagates along the circulation path with the mean flow. Assuming that the top (bottom) structure has a characteristic length $c\,l_t$ ($c\,l_b$), the pulse travels over a time $\tau_t = c\,l_t/U_t$ ($\tau_b = c\,l_b/U_b$), yielding a pulsation frequency $f_t = \tau_t^{-1}$ ($f_b = \tau_b^{-1}$). Our measurements, in agreement with the theory [39], indicate that the prefactor c acts as an approximately universal parameter that locks the two frequencies through the relation $U_t/(l_t f_t) = U_b/(l_b f_b)$. In this picture, a hot pulse emitted from the bottom roll triggers a corresponding hot pulse in the top roll (and analogously for a cold pulse). This mechanism explains both the doubling of the frequency when the effective circulation length is halved and the observed synchronization when asymmetric flow structures are imposed. It suggests that the flow pulsation, set by plume emission and advection, remains slaved to the mean convective velocity, providing a common "clock" that couples the different rolls despite their unequal scales.

We also examine the system's thermal response. Flow topology and BL thickness are theorized to strongly influence heat transfer [3], quantified by the Nusselt number Nu. Although some studies report a dependence of Nu on flow structure and symmetry [14,15,17], others find minimal effects when the LSC is absent or forced to lose coherence [18–20]. Our DNS results confirm that the presence of the barrier affects Nu by at most 2% relative to the no-barrier case (see Fig. 6), showing that heat transport is largely unaffected, even after the flow transitions to an axisymmetric structure with thinner boundary layers. The explanation for this insensitivity lies in the role of the thermal boundary layers [3,14]. For large-Pr fluids, the thermal BLs are nested within the thicker viscous BLs, making them less sensitive to changes in flow topology. In contrast, for low-Pr fluids, the thermal BL is thicker than the viscous BL and is therefore fully exposed to bulk flow modifications, making flow structures more likely to influence heat transport.

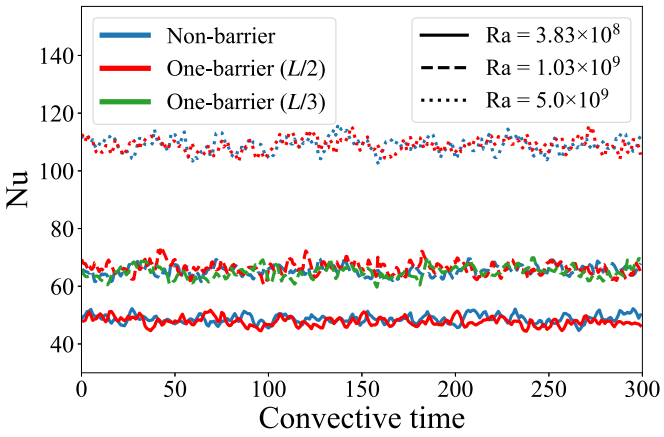


FIG. 6. Time evolution of the Nusselt number extracted from DNS for the midheight barrier case, compared with the no-barrier case. No significant variation is observed even after the flow-topology transition. A similar insensitivity is seen for the asymmetric case ($L/3$), and we expect the same trend for $L/4$ (not shown).

IV. CONCLUSION

We show that the hallmark structure of turbulent thermal convection, the LSC, possesses an internal "clock" $U/(lf) \approx 2.1$, relating characteristic velocity U to its pulsation frequency f and characteristic spatial scale l. This dimensionless number can be physically interpreted as the imposed shear U/l compared with the plume-shedding frequency f. The LSC can survive or be tripped in the presence of a thin ring-shaped sidewall barrier in a cylindrical cell. At low thermal

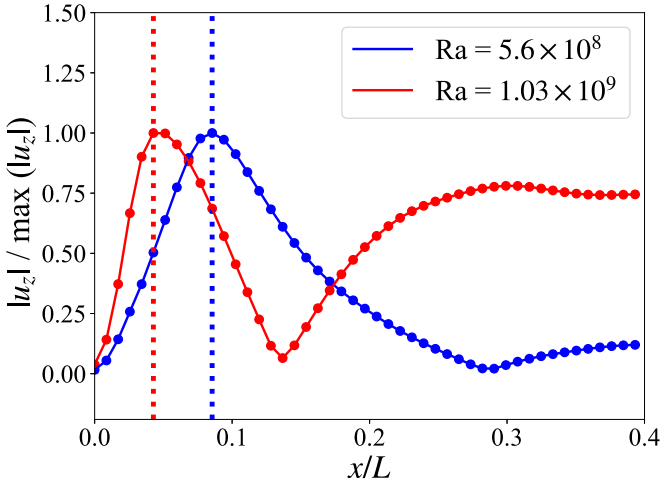


FIG. 7. Absolute near-wall vertical velocity profiles for a case before the transition (blue) and after the transition (red), both with the barrier placed at the sidewall. The boundary-layer profile is well resolved, with at least five velocity vectors across the layer. The dashed lines indicate the maxima of the profiles. The low-Ra case belongs to the $\delta_{u,L}$ group (before the transition), whereas the high-Ra case corresponds to $\delta_{u,L/2}$ (after the transition).

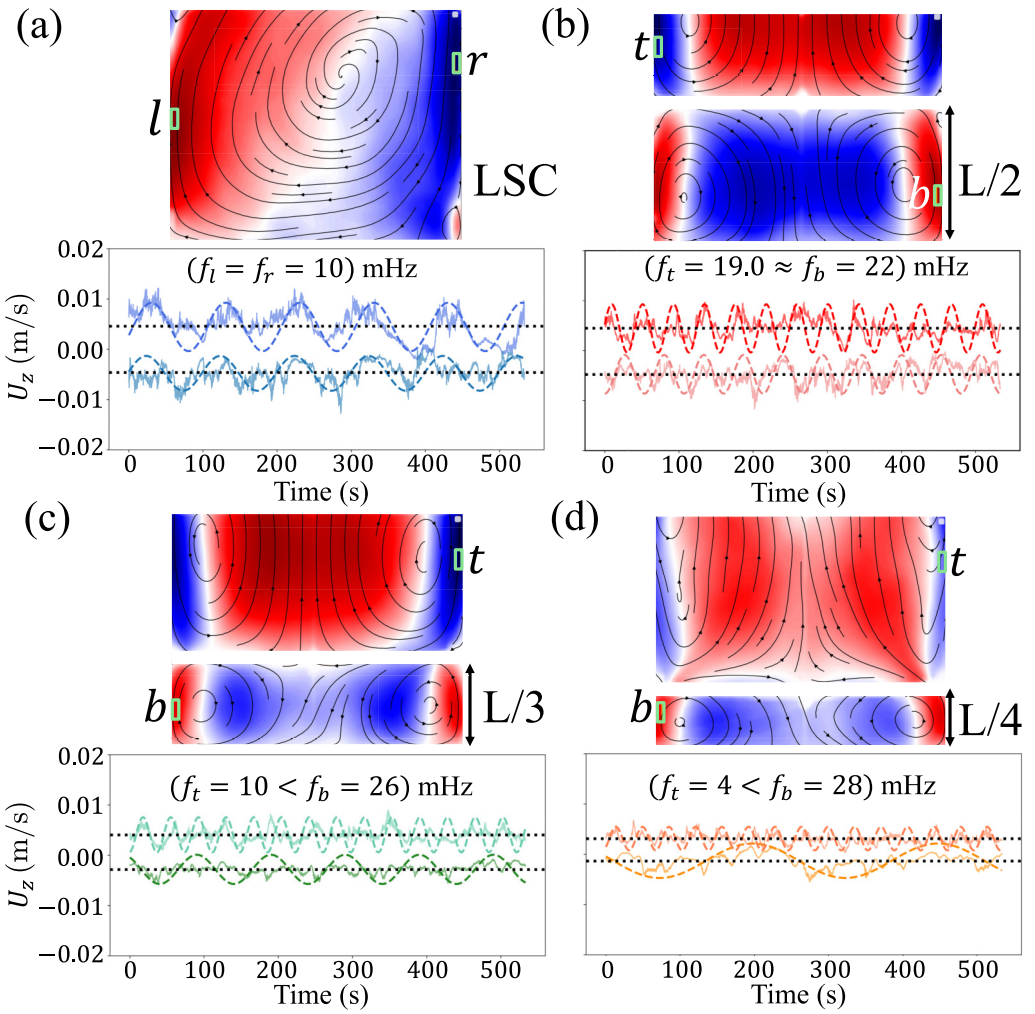


FIG. 8. Mean flow with the regions where the velocity was measured, highlighted with green boxes. The temporal series of the corresponding velocities in these regions are shown for the LSC [panel (a)] and for barriers at different heights from the bottom [panels (b)–(d)]. The principal frequency values are indicated in the figures. The colored dashed lines represent a sinusoidal function with a frequency equal to the dominant frequency of the real signal. The dotted black horizontal lines indicate the mean velocities of each time series: (a) $U_r \approx U_l \approx 0.0046\,\mathrm{m/s}$; (b) $U_t \approx 0.0045\,\mathrm{m/s}$, $U_b \approx 0.0047\,\mathrm{m/s}$; (c) $U_t \approx 0.003\,\mathrm{m/s}$, $U_b = 0.0041\,\mathrm{m/s}$; and (d) $U_t \approx 0.0013\,\mathrm{m/s}$, $U_b = 0.0031\,\mathrm{m/s}$. All the cases are at $\mathrm{Ra} = 1.03 \times 10^9$.

driving ($\mathrm{Ra} \lesssim 8 \times 10^8$), the LSC bypasses the barrier, sustained by thick kinetic boundary layers. At higher forcing ($\mathrm{Ra} \gtrsim 8 \times 10^8$), as the boundary layers thin to become comparable to the barrier scale, the flow transitions into a pair of vertically stacked, counterrotating, interconnected vortices. We find that, while the characteristic velocity remains largely unchanged (for the case $L/2$), the pulsation frequency adapts to conserve $U/(lf)$ for each of the two HCCs in view of the reduced characteristic length. The rolls behave as coupled oscillators, with this relation persisting even when they become asymmetric. In this way, we uncover a precise quantity linking plume pulsation and the flow structure, showing that topology control via geometric constraints in RBC provides a platform to reveal how turbulent flows reorganize and even synchronize. It is of great interest to assess the general validity of these principles when moving to more complex (geophysically or industrially inspired) domains and/or other convection liquids (including multilayer media; e.g., see Ref. [40]).

ACKNOWLEDGMENTS

This work is part of the project "Universal critical transitions in constrained turbulent flows" (File No. VI.C.232.026) within the NWO-Vici research program, funded by the Dutch Research Council (NWO). The authors also thank Gerald Oerlemans, Freek van Uittert, Jørgen van der Veen, and Chiel Koster for their technical support.

DATA AVAILABILITY

The data that support the findings of this article are openly available [41].

APPENDIX

Representative near-wall velocity profiles used to define the viscous boundary layers are shown in Fig. 7, with one case below and one above the transition. The vertical dotted lines

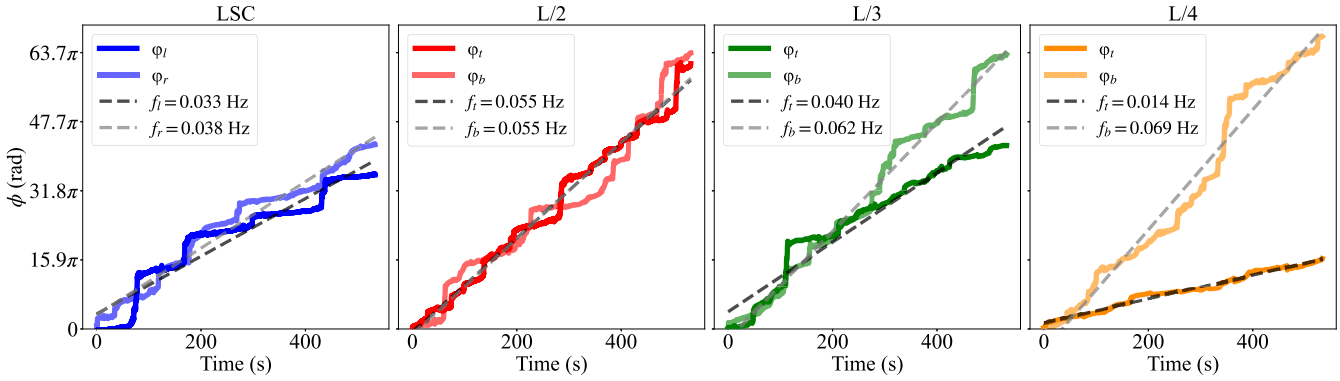


FIG. 9. Same as Fig. 5, but including linear fits to the phase evolution curves to extract an approximate mean frequency, $f_{\mathrm{inst},(t/b)}$, which is indicated in the figure legend.

mark the locations of the maxima; the distance from the wall to this position defines the boundary-layer thickness.

To analyze the pulsation frequency f in the system, we extract temporal series of the vertical velocity near the walls (see Fig. 8). The dominant frequency is extracted using the discrete Fourier transform, while the phase presented in the main text is obtained via the Hilbert transform. In the figure, the highlighted locations near the walls indicate where the temporal series are sampled, and the corresponding dominant frequencies are shown for the LSC case and for different barrier heights. These velocity samples are obtained directly from the PIV measurements in the measurement field. The regions highlighted in the figure serve as "virtual probes" near the walls, from which the velocity time series are extracted. The vertical positions are selected based on the locations where the maximum mean vertical velocities are observed.

As discussed in the main text, the frequency doubles after the transition when the barrier is placed at $L/2$ with respect to the LSC. In this case, the frequencies of the top and bottom rolls are similar, as are their phases, indicating synchronizationlike behavior. When asymmetry is introduced between the top and bottom rolls, the frequencies and phases no longer match. However, the relation $\frac{U_t}{l_t f_t}\left(\frac{U_b}{l_b f_b}\right)^{-1} \approx 1$ is still satisfied, which can be seen as a signature of generalized synchronization between the top and bottom parts (Table I).

The calculations presented in the first column of Table I were based on the principal frequency component extracted from the experimental measurements. Although this component reflects the global average frequency, it can still exhibit fluctuations; nevertheless, the resulting values remain reasonably close to 1. An alternative approach is to use the slope of a linear fit to the phase evolution over time, which provides an estimate of the instantaneous frequency of the signal (see Fig. 9, where $\varphi = 2\pi f_{\mathrm{inst}} t$). Using this approach, the results remain very close to 1 (see the second column of Table I), further supporting our argument of generalized synchronization, in which the two vortices are coupled in a complex but consistent manner.

[1] L. Rayleigh, LIX. On convection currents in a horizontal layer of fluid, when the higher temperature is on the under side, London, Edinburgh, Dublin Philos. Mag. J. Sci. **32**, 529 (1916).

[2] H. Bénard, Les tourbillons cellulaires dans une nappe liquide, Rev. Gén. Sci. Pure Appl. **11**, 1309 (1900).

[3] G. Ahlers, S. Grossmann, and D. Lohse, Heat transfer and large scale dynamics in turbulent Rayleigh-Bénard convection, Rev. Mod. Phys. **81**, 503 (2009).

[4] E. Villermaux, Memory-induced low frequency oscillations in closed convection boxes, Phys. Rev. Lett. **75**, 4618 (1995).

[5] E. Brown, A. Nikolaenko, and G. Ahlers, Reorientation of the large-scale circulation in turbulent Rayleigh-Bénard convection, Phys. Rev. Lett. **95**, 084503 (2005).

[6] C. Sun, H.-D. Xi, and K.-Q. Xia, Azimuthal symmetry, flow dynamics, and heat transport in turbulent thermal convection in a cylinder with an aspect ratio of 0.5, Phys. Rev. Lett. **95**, 074502 (2005).

[7] E. Brown and G. Ahlers, Rotations and cessations of the large-scale circulation in turbulent Rayleigh–Bénard convection, J. Fluid Mech. **568**, 351 (2006).

[8] Y. Tsuji, T. Mizuno, T. Mashiko, and M. Sano, Mean wind in convective turbulence of mercury, Phys. Rev. Lett. **94**, 034501 (2005).

[9] P. Wei, The persistence of large-scale circulation in Rayleigh–Bénard convection, J. Fluid Mech. **924**, A28 (2021).

[10] Y. Xie and K.-Q. Xia, Turbulent thermal convection over rough plates with varying roughness geometries, J. Fluid Mech. **825**, 573 (2017).

[11] S. Wagner and O. Shishkina, Heat flux enhancement by regular surface roughness in turbulent thermal convection, J. Fluid Mech. **763**, 109 (2015).

[12] S. Grossmann and D. Lohse, Scaling in thermal convection: A unifying theory, J. Fluid Mech. **407**, 27 (2000).

[13] R. J. A. M. Stevens, E. P. van der Poel, S. Grossmann, and D. Lohse, The unifying theory of scaling in thermal convection: the updated prefactors, J. Fluid Mech. **730**, 295 (2013).

[14] E. P. van der Poel, R. J. A. M. Stevens, and D. Lohse, Connecting flow structures and heat flux in turbulent Rayleigh-Bénard convection, Phys. Rev. E **84**, 045303(R) (2011).

[15] F. Schindler, S. Eckert, T. Zürner, J. Schumacher, and T. Vogt, Collapse of coherent large scale flow in strongly turbulent liquid metal convection, Phys. Rev. Lett. **128**, 164501 (2022).

[16] D. Lohse and O. Shishkina, Ultimate Rayleigh-Bénard turbulence, Rev. Mod. Phys. **96**, 035001 (2024).

[17] F. Xu, X.-S. Liu, X.-M. Li, and K.-Q. Xia, Restoration of axisymmetric flow structure in turbulent thermal convection by polymer additives, Phys. Rev. Lett. **134**, 084001 (2025).

[18] S. Ciliberto, S. Cioni, and C. Laroche, Large-scale flow properties of turbulent thermal convection, Phys. Rev. E **54**, R5901 (1996).

[19] K.-Q. Xia and S.-L. Lui, Turbulent thermal convection with an obstructed sidewall, Phys. Rev. Lett. **79**, 5006 (1997).

[20] K.-Q. Xia and X.-L. Qiu, Turbulent convection with "disconnected" top and bottom boundary layers, Europhys. Lett. **46**, 171 (1999).

[21] X.-L. Qiu and P. Tong, Onset of coherent oscillations in turbulent Rayleigh-Bénard convection, Phys. Rev. Lett. **87**, 094501 (2001).

[22] S. Cioni, S. Ciliberto, and J. Sommeria, Strongly turbulent Rayleigh–Bénard convection in mercury: Comparison with results at moderate Prandtl number, J. Fluid Mech. **335**, 111 (1997).

[23] C. Sun, K.-Q. Xia, and P. Tong, Three-dimensional flow structures and dynamics of turbulent thermal convection in a cylindrical cell, Phys. Rev. E **72**, 026302 (2005).

[24] M. Raffel, C. E. Willert, F. Scarano, C. J. Kähler, S. T. Wereley, and J. Kompenhans, *Particle Image Velocimetry: A Practical Guide*, 3rd ed. (Springer, Cham, 2018).

[25] R. Verzicco and P. Orlandi, A finite-difference scheme for three-dimensional incompressible flow in cylindrical coordinates, J. Comput. Phys. **123**, 402 (1996).

[26] R. Verzicco and R. Camussi, Numerical experiments on strongly turbulent thermal convection in a slender cylindrical cell, J. Fluid Mech. **477**, 19 (2003).

[27] T. Engels, D. Kolomenskiy, K. Schneider, and J. Sesterhenn, Numerical simulation of fluid–structure interaction with the volume penalization method, J. Comput. Phys. **281**, 96 (2015).

[28] L. Prandtl, Über Flüssigkeitsbewegung bei sehr kleiner Reibung, in *Verhandl. 3rd Int. Math. Kongr., Heidelberg, 1904* (Druck von BG Teubner, Leipzig, 1905).

[29] H. Blasius, *Grenzschichten in Flüssigkeiten mit kleiner Reibung* (Druck von BG Teubner, Leipzig, 1907).

[30] S. Wagner, O. Shishkina, and C. Wagner, Boundary layers and wind in cylindrical Rayleigh–Bénard cells, J. Fluid Mech. **697**, 336 (2012).

[31] H. Schlichting and K. Gersten, *Boundary-Layer Theory* (Springer, Berlin, 2016).

[32] C. Sun, Y.-H. Cheung, and K.-Q. Xia, Experimental studies of the viscous boundary layer properties in turbulent Rayleigh–Bénard convection, J. Fluid Mech. **605**, 79 (2008).

[33] N. C. Tai, E. S. C. Ching, L. Zwirner, and O. Shishkina, Heat flux in turbulent Rayleigh-Bénard convection: Predictions derived from a boundary layer theory, Phys. Rev. Fluids **6**, 033501 (2021).

[34] E. Brown, D. Funfschilling, and G. Ahlers, Anomalous Reynolds-number scaling in turbulent Rayleigh-Bénard convection, J. Stat. Mech. (2007) P10005.

[35] C. Sun and K.-Q. Xia, Scaling of the Reynolds number in turbulent thermal convection, Phys. Rev. E **72**, 067302 (2005).

[36] K.-Q. Xia, Two clocks for a single engine in turbulent convection, J. Stat. Mech. (2007) N11001.

[37] J. H. Lienhard, *Synopsis of Lift, Drag, and Vortex Frequency Data for Rigid Circular Cylinders* (Technical Extension Service, Washington State University, Pullman, 1966), Vol. 300.

[38] A. Pikovsky, M. Rosenblum, and J. Kurths, *Synchronization: A Universal Concept in Nonlinear Sciences*, Cambridge Nonlinear Science Series (Cambridge University Press, Cambridge, 2001).

[39] S. Grossmann and D. Lohse, Fluctuations in turbulent Rayleigh–Bénard convection: The role of plumes, Phys. Fluids **16**, 4462 (2004).

[40] M. Wang, X. Y. Chen, W. Wang, and P. Wei, Heat transport and flow structure in thermal convection with two liquid layers, J. Fluid Mech. **978**, A4 (2024).

[41] L. Martnez-Ortz, Y. H. Lemm, H. J. H. Clercx, and R. P. J. Kunnen, Repository for: "The Persistent Clock of Turbulent Thermal Convection" [Data set]. Zenodo (2025), https://doi.org/10.5281/zenodo.17395513.